Progressive Inter-scale and Intra-scale Non-blind Image Deconvolution

Lu Yuan[1]   Jian Sun[2]   Long Quan[1]   Heung-Yeung Shum[2]

[1]The Hong Kong University of Science and Technology   [2]Microsoft Research Asia

Figure 1: *Non-blind deconvolution. From left to right: input blurred image and blur kernel (estimated from the blurred image using [Fergus et al. 2006]), standard Richardson-Lucy (RL) [Lucy 1974] result, and our result.*

Abstract. Ringing is the most disturbing artifact in the image deconvolution. In this paper, we present a progressive inter-scale and intra-scale non-blind image deconvolution approach that significantly reduces ringing. Our approach is built on a novel edge-preserving deconvolution algorithm called *bilateral Richardson-Lucy (BRL)* which uses a large spatial support to handle large blur. We progressively recover the image from a coarse scale to a fine scale (inter-scale), and progressively restore image details within every scale (intra-scale). To perform the inter-scale deconvolution, we propose a *joint bilateral Richardson-Lucy (JBRL)* algorithm so that the recovered image in one scale can guide the deconvolution in the next scale. In each scale, we propose an iterative residual deconvolution to progressively recover image details. The experimental results show that our progressive deconvolution can produce images with very little ringing for large blur kernels.

1 Introduction

The goal of image deconvolution/deblurring is to reconstruct a true image I from a degraded image B that is the convolution of the true image and a spatial invariant/variant kernel K:

$$B = \text{noise}(I \otimes K), \qquad (1)$$

where $\otimes$ is the convolution operator, and $\text{noise}(\cdot)$ is the noise process. The problem is called *blind deconvolution* if both kernel and image are unknown, or *non-blind deconvolution* if only the image is unknown. The image deconvolution is not only critical to many scientific applications such as astronomical imaging, remote sensing, and medical imaging, but also important for consumer photography and computational photography.

In consumer photography, image blurring is often unavoidable due to insufficient lighting, use of a telephoto lens, or use of a small aperture for a wide depth of field. As resolution increases, camera manufacturers have begun to compete on the basis of mechanical image stabilization. In computational photography, the captured image is usually a convolved image that needs to be deconvolved, for instances, in coded exposure [Raskar et al. 2006], masked aperture [Levin et al. 2007; Veeraraghavan et al. 2007], multi-aperture [Green et al. 2007], light field microscopy [Levoy et al. 2006], and wavefront coding [Dowski and Johnson 1999].

However, the deconvolved image usually contains unpleasant deconvolution artifacts due to the ill-posedness of the deconvolution even if the kernel is known. Because the kernel is often band-limited with a sharp frequency cut off, there will be zero values or near-zero values in its frequency response. At those frequencies, the direct inverse of the kernel usually has a very large magnitude, causing excessive amplification of signal and noise. The two most prevalent resulting artifacts are ripple-like ringing around the edges and amplified noise. Ringing artifacts are periodic overshoots and undershoots around the edge, which decay spatially away from the edge, as shown in the middle of Figure 1. It is extremely difficult to remove these artifacts after the deconvolution. Moreover, we cannot obtain the true kernel in practice. The inaccurate kernel will also amplify the artifacts and result in undesired image structures.

In this paper, we focus on non-blind deconvolution. In many scientific applications, the kernel is known. In the computational photography systems, the kernel is usually known or known up to a scale. For consumer photography, there are a number of effective ways to estimate the kernel. For instance, the kernel due to the camera motion can be effectively estimated from a single image [Fergus et al. 2006], from a secondary sensor [Ben-Ezra and Nayar 2003], from a secondary image [Yuan et al. 2007], from an accelerometers, or from a gyroscopes [Invensense.com]. The kernel due to simple object motion such as 1D motion, affine transformation, or in-plane rotation, can be estimated automatically or interactively [Raskar et al. 2006; Levin 2006; Jia 2007].

To reduce undesirable artifacts, edge regularization techniques [Terzopoulos 1986; Rudin et al. 1992; Geman and Yang 1995; Black et al. 1998; Dey et al. 2006; Levin et al. 2007] have been proposed using a non-Gaussian prior on the image to add strong regularization for the smooth regions and weak regularization for the sharp edges. Thus, the sharp edges are preserved while the ringing artifacts are reduced.

Unfortunately, the current edge preserving methods only work well for relatively small kernels (e.g., <15 pixels) because these meth-

ods need to first locate the image edges in the initial blurred image or the image recovered in each iteration. If the blur kernel is large, locating the image edges in the first iteration becomes difficult. Consequently, inappropriate regularization yields poor results.

Our approach. We propose a progressive inter-scale and intra-scale non-blind deconvolution that preserves the edges and reduces the ringing artifacts, especially for the large kernel. First, we progressively perform the deconvolution in the scale space. At the coarsest scale, we are able to obtain reasonably good edges as the kernel is small. Using the recovered edges in one scale as a guide, we can more accurately locate the edges in the finer scale. Thus, we progressively apply an appropriate regularization from coarse to fine so that the sharp edges in the finest scale can be eventually recovered. Second, in each scale, we also progressively carry out the deconvolution by an iterative residual deconvolution algorithm. This algorithm gradually recovers more and more image details/edges which could not been recovered in the previous scale.

The above inter-scale and intra-scale deconvolution relies on a novel deconvolution algorithm called *joint bilateral Richardson-Lucy (JBRL)*. The JBRL preserves the edges by taking both the image itself and a guide image into account. The guide image is the recovered image from the previous scale in the inter-scale deconvolution, or the restored image from the previous iteration in the intra-scale deconvolution. The JBRL algorithm is built on a proposed, more fundamental edge-preserving algorithm called *bilateral Richardson-Lucy (BRL)*, which introduces a bilateral regularization by borrowing the idea of bilateral filtering [Tomasi and Manduchi 1998; Durand and Dorsey 2002]. The BRL can handle larger blur kernels because it uses a much larger spatial support.

By performing our progressive intra-scale and inter-scale deconvolution, we can recover the sharp edges and fine details while substantially suppress the ringing artifacts, as shown in Figure 1.

2 Related work

Non-blind deconvolution. There is an abundant literature on the non-blind deconvolution. The reader is referred to [Banham and Katsaggelos 1997] for classical methods, such as Wiener filter, Kalman filter, and Tikhonov regularization [Tikhonov 1943]. In this paper, we focus on the work most relevant to ours.

Edge-preserving regularization [Geman and Reynolds 1992] gives limited or small penalties on large image edges according to a non-Gaussian prior, e.g., TV regularization [Rudin et al. 1992; Dey et al. 2006]. In [Levin et al. 2007], excellent results are obtained using a sparse, natural image prior which encouraging the majority of image pixels piecewise smooth. Other priors include controlled continuity function [Terzopoulos 1986] and half-quadratic function [Geman and Yang 1995]. See [Black et al. 1998] for a summary for various robust functions.

Image edges can also be preserved by explicitly introducing segmentation. [Mignotte 2006] uses the adaptive regularization, partitioning the image into homogeneous regions during each iteration. Bar et al. [2006] couple the deconvolution and segmentation using a Mumford-Shah regularization.

Most multi-scale deconvolution methods [Murtagh et al. 1995; Neelamani et al. 2004; Figueiredo et al. 2007] operate in the wavelet domain. Essentially, these approaches also try to preserve the edges by adaptive regularization on the wavelet coefficients.

The above approaches share a common weakness: if the blur kernel is large, it is difficult to find edges in the blurred image or the restored image in each iteration.
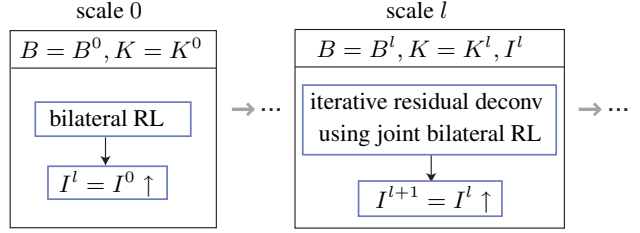

Figure 2: *Progressive deconvolution. The image is progressively reconstructed from coarse scale to fine scale. At the top scale 0, we recover and upsample the deconvoluted image using the bilateral RL algorithm. At each scale l, we apply the iterative residual deconvolution (which is based on the joint bilateral RL algorithm) to progressively recover image details.*

Blind deconvolution. A comprehensive literature review for the blind deconvolution can be found in [Kundur and Hatzinakos 1996]. Early works [Reeves and Mersereau 1992; Caron et al. 2002] usually only handle a simple parametric form of the kernel. Later, Fergus et al. [2006] showed that a very accurate kernel can be estimated for blur due to camera shake by using natural image statistics together with a sophisticated variational Bayes inference algorithm. They recover the image using the standard Richardson-Lucy (RL) algorithm [Lucy 1974]. Spatially variant kernel estimation has also been studied in [Bardsley et al. 2006; Levin 2006]

Deconvolution in computational photography. The deconvolution is an essential component in one branch of computational photography: computational optics, which captures optically coded (convolved) images followed by computational decoding (deconvolution) to produce new images. For example, a coded aperture in time is used for motion deblurring [Raskar et al. 2006] and image super-resolution [Agrawal and Raskar 2007], and a coded aperture in space is used for depth estimation and refocusing [Levin et al. 2007; Veeraraghavan et al. 2007; Green et al. 2007], modulated light field capturing [Veeraraghavan et al. 2007], and improving the pinhole camera in astronomy [Zand 1996]. In light field microscopy [Levoy et al. 2006], the 3D volume is reconstructed from a focal stack by a 3D deconvolution. In wavefront coding [Dowski and Johnson 1999], the final image is deconvolved from a depth-independent out-of-focus image.

3 Overview

In this section, we present an overview of our progressive deconvolution framework. We build a pyramid $\{B^l\}_{l=1}^{L}$ of the full-resolution blurred image B, and a pyramid $\{K^l\}_{l=1}^{L}$ of the blur kernel K using bicubic downsampling and scale factor of $\sqrt{2}$. Our goal is to progressively recover an image pyramid $\{I^l\}_{l=1}^{L}$ from coarse to fine. Figure 2 is the flowchart and Figure 3 shows an example.

At the top scale 0, we directly apply the proposed bilateral RL (BRL) algorithm (Section 4). The recovered image at this scale contains few ringing artifacts because the BRL algorithm can effectively suppress the ringing when the kernel is relatively small. Then, we upsample the image for the next scale using the BRL algorithm again.

At each scale l, we use the upsampled result I^l from the previous scale as a *guide* image. We apply the joint bilateral RL (JBRL) algorithm (Section 5.1) which uses guide image I^l to guide the deconvolution. Moreover, we progressively recover the image details by an iterative residual deconvolution algorithm (Section 6.1). The coarse details are first recovered using strong regularization strength, and the fine details are later restored using weak regularization strength,
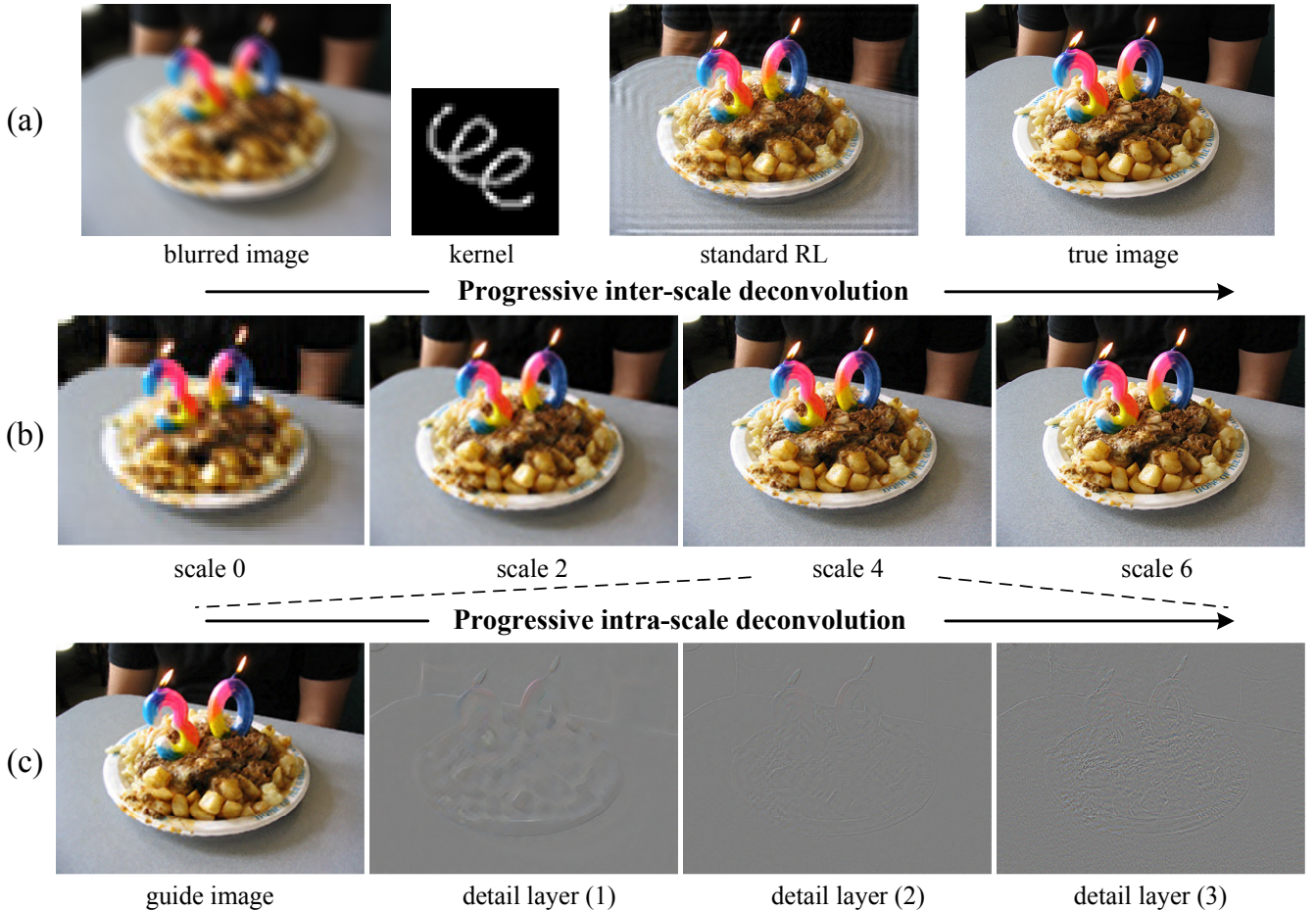
Figure 3: *Progressive deconvolution example. (a) from left to right: blurred image, blur kernel, result by standard RL algorithm, and ground truth image. (b) progressively recovered images from coarse scale to fine scale by our approach. (c) in each scale, the guide image is the upsampled image from the previous scale. The image details are progressively recovered. The numbers in braces are the iteration steps. Compared with the standard RL result, our final result (scale 6 in (b)) contains much fewer ringing artifacts.*

as shown in Figure 3 (c). Finally, we upsample the resulting image for the next scale.

Using the above progressive inter-scale and intra-scale deconvolution, we gradually recover an image with few ringing artifacts, as shown in Figure 3(b).

4   Bilateral Richardson-Lucy (BRL)

We first revisit the Richardson-Lucy (RL) deconvolution algorithm [Lucy 1974], then introduce our edge-preserving deconvolution algorithm which we call bilateral Richardson-Lucy (BRL). BRL is the building block of our progressive deconvolution framework.

Richardson-Lucy (RL). For a Poisson noise distribution, the likelihood probability of the image I can be expressed as:

$$p(B|I) = \prod_x \frac{(I \otimes K)(x)^{B(x)} \exp\{-(I \otimes K)(x)\}}{B(x)!}, \quad (2)$$

where $B_p = \text{Poisson}((I \otimes K)(x))$ is a Poisson process for each pixel x. For simplicity, we omit x in the following equations. The maximum likelihood solution of I can be obtained by minimizing

the following energy:

$$I^* = \arg\min_I E(I), \quad (3)$$

where

$$E(I) = \sum \left\{ (I \otimes K) - B \cdot \log[(I \otimes K)] \right\}. \quad (4)$$

Taking the derivative of $E(I)$ and assuming the normalized kernel K ($\int K(x)dx = 1$), the Richardson-Lucy (RL) algorithm [Lucy 1974] iteratively updates the image according to:

$$I^{t+1} = I^t \left[K^* \otimes \frac{B}{(I^t \otimes K)} \right], \quad (5)$$

where K^* is the adjoint of K, i.e, $K^*(i,j) = K(-j,-i)$, and t is a time step. The RL algorithm has two important properties: non-negativity and energy preserving. The non-negativity constrains estimated values be negative. The algorithm preserves the total energy of the image in the iteration. These two properties give the superior performance of the RL algorithm. In addition, the RL algorithm is efficient; it requires only two convolutions and two multiplications per iteration.

4.1 Bilateral Richardson-Lucy (BRL)

The RL algorithm does not preserve the edges in the design of the regularization. So we add a new edge-preserving regularization term $E_B(I)$ to the energy (3):

$$I^* = \arg \min_I [E(I) + \lambda E_B(I)], \tag{6}$$

where λ is the regularization factor. We define the term $E_B(I)$ as:

$$E_B(I) = \sum_x \sum_{y \in \Omega} f(|x - y|)\rho(|I(x) - I(y)|), \tag{7}$$

where $f(\cdot)$ is the spatial filter and $\rho(\cdot)$ is the robust penalty function. We take a Gaussian for the spatial filter

$$f(|x - y|) = \exp\left(-\frac{|x - y|^2}{2\sigma_s}\right).$$

The spatial support Ω centered at each pixel x controls the amount of neighboring pixels involved. We adaptively set the radius of spatial support r_Ω to match the size of the blur kernel: $r_\Omega = 0.5r_K$, where r_K is the radius of the blur kernel. The spatial variance σ_s could be derived from the radius r_Ω: $\sigma_s = (r_\Omega/3)^2$.

For the robust function $\rho(\cdot)$, we choose the following form:

$$\rho(|I(x) - I(y)|) = 1 - \exp\left(-\frac{|I(x) - I(y)|^2}{2\sigma_r}\right).$$

It gives a large but limited penalty on the image difference $|I(x) - I(y)|$ for the range variance σ_r. We adaptively set the range variance to $0.01 \times |\max(I) - \min(I)|^2$ by following [Kopf et al. 2007].

By minimizing (6), we get a regularized version of RL algorithm:

$$I^{t+1} = \frac{I^t}{1 + \lambda \nabla E_B(I^t)} \left[K^* \otimes \frac{B}{(I^t \otimes K)}\right]. \tag{8}$$

The derivative $\nabla E_B(I)$ can be computed efficiently by:

$$\nabla E_B(I) = \sum_{y \in \Omega} \left(I_y^d - I_y^d D_y\right), \tag{9}$$

where D_y is the displacement matrix (operator) which shifts the entire image I_y^d by $|\vec{e}|$ pixels in the direction of $\vec{e}$. Here, $\vec{e}$ denotes the displacement vector from each pixel x to its neighbor pixel y. I_y^d is a weighted long-range gradient image in the direction of $\vec{e}$. For each pixel x in the image I_y^d,

$$I_y^d(x) = f(|x - y|)g(|I(x) - I(y)|) \cdot \frac{(I(x) - I(y))}{\sigma_r}, \tag{10}$$

where the range filter $g(|I(x) - I(y)|) = 1 - \rho(|I(x) - I(y)|) = \exp(-\frac{|I(x)-I(y)|^2}{2\sigma_r})$ is a Gaussian filter. The weight for the difference $|I(x) - I(y)|$ is computed by a bilaterally weighted filter $f(\cdot)g(\cdot)$ in image and range, also called bilateral filter [Tomasi and Manduchi 1998; Durand and Dorsey 2002].

The gradient image I_y^d controls the regularization of each pixel. Without the bilateral filter, I_y^d would place a large penalty on large image gradient, so the process would smooth the sharp edges. The bilateral filter, however, preserves the sharp edges because it takes on smaller values as the spatial distance and/or the range distance increase. Because we apply a bilateral regularization term in (7), we call the deconvolution algorithm in (8), *bilateral Richardson-Lucy (BRL)*.

Tikhonov regularization   TV regularization

Levin's method   our approach
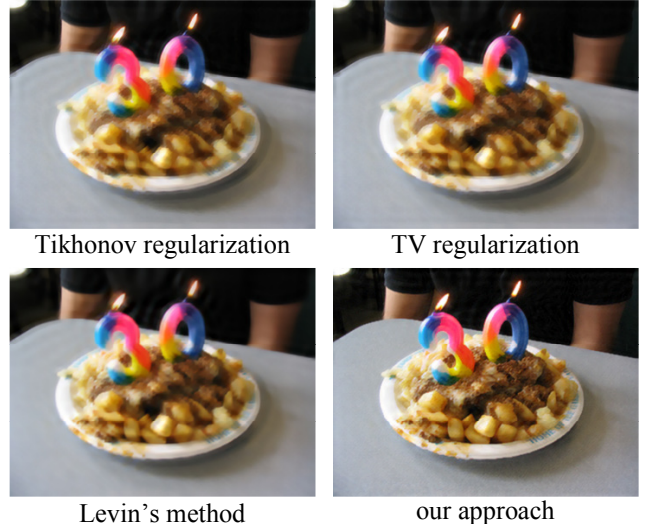
Figure 4: *Comparison of three regularization algorithms. Our approach is able to recover more image details.*

The BRL adaptively uses the information in a *large* spatial support (11×11 in this case). Figure 4 shows the comparison of five deconvolution algorithms: standard RL, Tikhonov regularization, TV regularization [Dey et al. 2006], Levin's method [Levin et al. 2007], and our algorithm. In this example, we downsample the blurred image so that the blur kernel size is about 15 pixels. The results show that BRL preserves image edges well, suppresses ringing artifacts, and recovers more image details.

Although using a larger spatial support helps, blurred images with large blur kernels are still beyond the capability of the BRL algorithm. Figure 5 (a) shows the BRL result for 40×40 kernel. Details are also suppressed. In the next two sections, we present a progressive deconvolution approach which is capable of effectively handling large blur kernels.

5 Progressive Inter-scale Deconvolution

The basic idea of progressive deconvolution is to use an image as guide for the deconvolution. In the inter-scale level, we use the image recovered in the one scale as the guide image for the deconvolution in the next scale. In the intra-scale level, we use the image restored in one iteration as the guide image for the next iteration. In this section, we first introduce the inter-scale deconvolution.

Figure 3 (a) shows a blurred image with a 40×40 blur kernel. The leftmost image (scale 0) in Figure 3 (b) is the deconvolution result by the BRL at the coarsest scale. As we can see, this coarse scale image provides more useful edge information than the original blurred image. If we may exploit the information from this image for the deconvolution in the next scale, we can obtain a better result. If we continue the process from coarse to fine, better result at the finest scale can be obtained.

To exploit the edge information in the guide image, we propose a joint bilateral RL (JBRL) algorithm as follows, motivated by the successful joint bilateral filtering in [Petschnigg et al. 2004; Eisemann and Durand 2004; Kopf et al. 2007].

5.1 Joint Bilateral Richardson-Lucy (JBRL)

Let the upsampled image from the previous scale be the guide image I^g. We change the new regularization term that we introduced in the above section to a joint term $E_{JB}(I; I^g)$ that takes both the

Figure 5: *Results on a 40×40 kernel. (a) bilateral RL (BRL). (b) progressive inter-scale deconvolution using joint bilateral RL (JBRL). More details are recovered. (c) progressive inter-scale and intra-scale deconvolution. Much finer details are restored. (d) true image.*

image and the guide image into account:

$$E_{JB}(I; I^g) =$$
$$\sum_x \sum_{y \in \Omega} f(|x - y|)g'(|I^g(x) - I^g(y)|)\rho(|I(x) - I(y)|), \text{(11)}$$

where $g'(|I^g(x) - I^g(y)|)$ is the range filter applied on the guide image I^g. We also use a Gaussian for this range filter:

$$g'(|I^g(x) - I^g(y)|) = \exp\left(-\frac{|I^g(x) - I^g(y)|^2}{2\sigma_r^g}\right),$$

where σ_r^g is the range variance, which is adaptively set to $0.01 \times |\max(I^g) - \min(I^g)|^2$. To reconstruct the image, we minimize:

$$I^* = \arg \min_I [E(I) + \lambda E_{JB}(I; I^g)]. \quad \text{(12)}$$

The derivation of corresponding RL algorithm is the same except that Equation (10) became:

$$I_y^d(x) = f(|x - y|)g(|I(x) - I(y)|) \cdot$$
$$g'(|I^g(x) - I^g(y)|) \cdot \frac{(I(x) - I(y))}{\sigma_r}. \quad \text{(13)}$$

The additional range filter $g'(|I^g(x) - I^g(y)|)$ decreases the regularization at places where the image gradient $|I^g(x) - I^g(y)|$ is large in the guide image I^g. Thus, the regularization is adaptively guided by two kinds of forces: the "internal force" $g(|I(x) - I(y)|)$ from the image itself and the "external force" $g'(|I^g(x) - I^g(y)|)$ from the guide image. Figure 6 shows the effectiveness of the joint bilateral RL.

Figure 5 (b) shows the progressive inter-scale deconvolution result which is better than the BRL result in Figure 5 (a). However, many details are not be recovered. In the next section, we introduce the intra-scale deconvolution to restore more fine details in each scale.

Upsampling with BRL In a typical scale space approach, the solution in one scale is upsampled for the next scale, usually by a simple bilinear or bicubic interpolation schema. These methods tend to smooth the edges, so are insufficient for our approach. We adopt the BRL to upsample the image as follows. We assume that the bicubic upsampled image I^u is a degraded version of the intended hi-resolution I^h. The degradation is approximated by a small Gaussian blur kernel k: $I^u = I^h \otimes k$ with the standard deviation of 0.5 for the upsampling factor $\sqrt{2}$. We found that the approximation gives very good results for our purpose of producing an upsampled image with sharp edges.

6 Progressive Intra-scale Deconvolution

The progressive inter-scale deconvolution only focus on the location of the edge but not the edge strength or scale. In fact, the image with strong edges requires large global regularization strength


residual blurred image	guide image

bilateral RL	joint bilateral RL
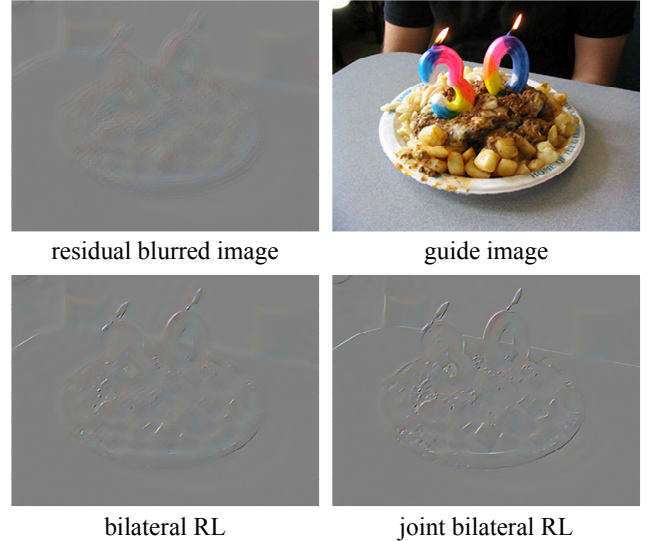
Figure 6: *Joint bilateral RL. Top: residual blurred image ΔB and guide image I^g. Bottom: deblurred residual layers ΔI by bilateral RL and joint bilateral RL. The latter recovers more details.*

(λ) to effectively suppress the ringing in the smooth regions because the magnitude of ringing artifact is usually proportional to the amplitude of the jumping edges. However, large regularization strength will also suppress the detail recovery. Therefore, we propose a progressive intra-scale deconvolution to recover image details step-by-step by decreasing the regularization strength, using an iterative residual deconvolution as follows.

6.1 Iterative residual deconvolution

The residual deconvolution proposed in [Yuan et al. 2007] performs the deconvolution on the relative image to reduce the absolute amplitude, and so to reduce the resulting ringing artifacts. We integrate this idea into an iterative deconvolution scheme that progressively recovers image details while decreasing the regularization strength. The algorithm is described in Figure 7.

In each iteration, we first compute the blurred residual image $\Delta B = B - I^g \otimes K$. Then, we apply the joint bilateral RL to recover the detail layer ΔI from the blurring equation $\Delta B = \Delta I \otimes K$. The image I^g is first used as the guide image in the joint bilateral RL algorithm, and then is updated with recovered layer of details ΔI for the next iteration.

This amounts to minimizing the following energy by decreasing the regularization strength λ during iterations:

$$\Delta I^* = \arg \min_{\Delta I}[E(\Delta I) + \lambda E_{JB}(\Delta I; I^g)], \text{ with } \lambda^{t+1} = \gamma \lambda^t,$$
$$\text{(14)}$$
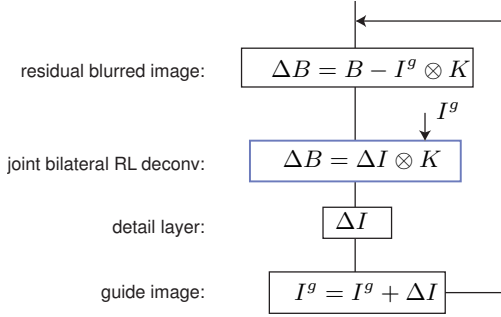
Figure 7: *Iterative residual deconvolution. First, we calculate a residual blurred image ΔB using the guide image I^g which is computed from the previous scale. Second, the detail layer ΔI is recovered by the joint bilateral RL (JBRL) with the help from the guide image I^g. Last, the guide image I^g is updated by adding the new recovered detail layer.*

where γ is a decay factor. In our implementation, we set the decay factor to $\frac{1}{3}$ and iterate three times to recover three layers of details. As shown in Figure 3 (c), each iteration recovers a layer of image details and the layers represent finer and finer image details.

Hi-pass JBRL for ringing suppression In the last iteration (the third one), the regularization strength decreases to $\frac{\lambda}{9}$ and becomes too small to effectively suppress ringing. We find that the frequencies of the most noticeable ringing artifacts are usually lower than the frequencies of the details that we want to recover in the last iteration. Furthermore, human perception tolerates small scale ringing in highly textured regions. Based on this observation, we add an energy term $E_H(\Delta I)$ to enforce a smoothness constraint on the middle range of frequencies of the recovered details:

$$\Delta I^* = \arg\min_I [E(\Delta I) + \lambda E_J(\Delta I; I^g) + \beta E_H(\Delta I)], \quad (15)$$

where β is a scale parameter set to 0.4λ. The term $E_H(\Delta I) = \sum_x \Delta I \otimes G$ is the sum of filtered image $\Delta I \otimes G$ by a Gaussian kernel G with the variance $\sigma_h = \sigma_s$. In other words, we add a mid-scale regularization term to suppress the most unpleasant mid-scale ringing artifacts while allow the recovery of fine details. We only add this regularization in the last iteration. Figure 8 shows the results with and without the energy term $E_H(\Delta I)$, and extracted the ringing layer.

Figure 5 (c) shows the result by our final inter-scale and intra-scale deconvolution and the intra-scale deconvolution. Much more details are recovered with the intra-scale deconvolution, compared with the results in Figure 5 (a) and (b).

7 Experimental Results

We apply our progressive deconvolution on a variety of real images. 11, Figure 12 and 13 are three image blurred due to camera shake: a painting in the museum, an outdoor photographer, and a toy monkey. We estimate the blur kernels of these images by Fergus's single image method [Fergus et al. 2006]. The estimated kernel sizes are 27×27, 38×38 and 39×39 respectively.

In our experiments, we generally set the spatial variances to the default values and adaptively set the range variances in bilateral RL and joint bilateral RL. The regularization factor λ balances the details recovery and ringing suppression. For the example in Figure 11, we use a large value 0.05 since the contrast in this image is high. For other examples, we use the default value 0.03.

The toy monkey in Figure 11 is taken by a telephoto len with effective 320mm focal length (200mm lens on a DSLR with 1.6 cropping


residual blurred image   joint bilateral RL

hi-pass, joint bilateral RL   ringing layer
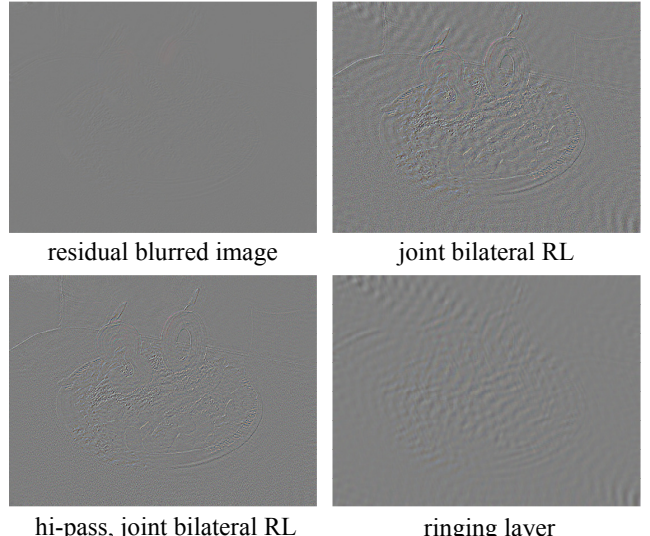
Figure 8: *Hi-pass JBRL in the last iteration at the scale 5. The ringing layer is computed by subtracting the hi-pass JBRL result from the JBRL result. All images are enhanced for display.*

factor). The image is blurred even with the shutter speed 1/15 secs and 5.0 aperture. Our approach produces a high quality, natural looking image compared with standard RL.

In Figure 12, we compare our approach with four leading methods: standard RL, TV regularization [Dey et al. 2006], Levin's method [Levin et al. 2007], and wavelet regularization [Murtagh et al. 1995]. For the standard RL, we run 20 iterations. For the other three methods, we fine tune their regularization factors to produce the most visually pleasant results by balancing the detail recovery and ringing reduction. Standard RL produces the most noticeable ringing. The three regularization methods reduce the ringing artifacts to a certain degree, but also suppress or blur the image details. Our approach can recover finer image details and thin image structures while successfully suppress ringing.

Figure 13 shows cropped views of an outdoor scene. We show the result by standard RL and TV regularization for the comparison in the paper. A full comparison is in the supplementary material. As we can see, the camera, tripod, and shutter release cable are well reconstructed. The subtle color noises in our result can be removed by post-processing in the chrominance channels, but we show the raw deconvolution result here.

In Figure 14, we apply our approach on two examples from [Fergus et al. 2006]. The blurred images and estimated kernels are obtained from author's website[1]. Note that the main contributions of [Fergus et al. 2006] are on kernel estimation and they use the standard RL for the non-blind deconvolution. In this paper, we provide a new non-blind deconvolution algorithm which can further improve the quality of the recovered image. The combination of the two approaches is a powerful solution for single image deblurring.

We also apply our approach to an example from [Yuan et al. 2007]. Figure 15(a) is the blurred image and Figure 15(b) is the result from [Yuan et al. 2007] in which a blurred/noisy image pairs are used. Figure 15(c) is the result by combing Fergus et al's kernel estimation and our non-blind deconvolution only using a single blurred image as the input. The obtained result is comparable to the result by the Yuan et al's two image approach.

---

[1] *http://cs.nyu.edu/fergus/research/deblur/*
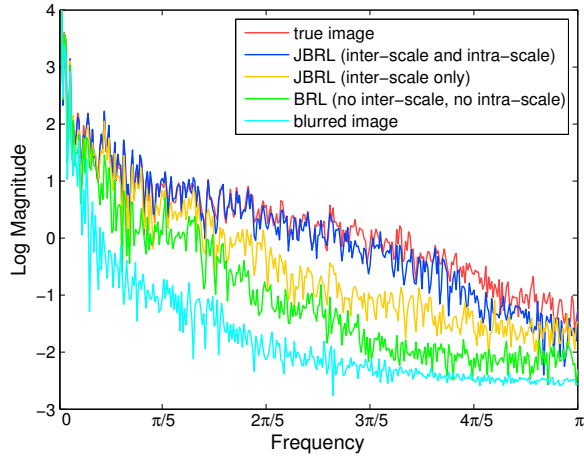
Figure 9: *The DFT curves of a 1D scanline in 5 images: true image, blurred image, deconvolved results by BRL (no inter-scale, no intra-scale), by JBRL (inter scale only) and JBRL (inter-scale and intra-scale).*

Figure 10: *Limitations. Top: our result on a 160×160 motion blur kernel. Boundary artifacts appear. Bottom: our result on a 40×40 gaussian kernel. High frequency details destroyed in the blurring process cannot be recovered.*

8 Discussion

Frequency analysis. To better understand the effectiveness of the inter-scale and intra-scale deconvolution, we perform an analysis in the frequency domain. We compute one-dimensional Discrete Fourier Transform (DFT) of a scanline (262th row) in four images shown in Figure 5 and the corresponding blurred image. The DFT curves of five scanlines are compared in Figure 9. The main conclusion drawn from the figure is that all three techniques we proposed - BRL, inter-scale deconvolution, and intra-scale deconvolution play important roles in recovering of high frequency contents.

Limitations. What is the largest kernel size in the capability of our approach? It depends on the image size and the frequency spectrum of the blur kernel. When the kernel size is approaching the image size, the boundary effect will arise. Figure 10 (top) shows the recovered result using a very large motion blur kernel 160×160, for the image size of 700×525. The system is severely under-constrained because more unknown pixels outside the image contribute to the blurred image.

The frequency spectrum of the blur kernel also determines how much image details we are able to recover. In Figure 10 (bottom), we apply our approach on the blurred image with a 40×40 gaussian kernel. Most high-frequency components have already lost in the low-pass blurring procedure. We can successfully suppress the ringing artifacts but are not able recover all image information due to the frequency loss.

9 Conclusion

The image deconvolution is an important and long-standing problem for many applications. In this paper, we have presented a progressive inter-scale and intra-scale non-blind image deconvolution approach. We have developed two novel edge-preserving deconvolution algorithms, bilateral RL and joint bilateral RL, to make the progressive deconvolution effective. The results obtained by our approach show that a combination of progressive inter-scale and intra-scale deconvolution can recover visually pleasing images with very little no ringing.

In the future, we plan to extend our approach to 3D deconvolution [Levoy et al. 2006]. We are also interested to apply the progressive framework to other restoration problems requiring edge preservation, such as image denoising or surface reconstruction.

Acknowledgements

References

AGRAWAL, A., AND RASKAR, R. 2007. Resolving objects at higher resolution from a single motion-blurred image. In *Proceedings of CVPR*, 1–8.

BANHAM, M. R., AND KATSAGGELOS, A. K. 1997. Digital image restoration. *IEEE Signal Processing Magazine 42*, 2, 24–41.

BAR, L., SOCHEN, N., AND KIRYATI, N. 2006. Semi-blind image restoration via mumford-shah regularization. *IEEE Trans. on Image Processing. 15*, 2, 483–493.

BARDSLEY, J., JEFFERIES, S., NAGY, J., AND PLEMMONS, R. 2006. Blind iterative restoration of images with spatially-varying blur. In *Optics Express*, 1767–1782.

BEN-EZRA, M., AND NAYAR, S. K. 2003. Motion deblurring using hybrid imaging. In *Proceedings of CVPR*, vol. I, 657–664.

BLACK, M. J., SAPIRO, G., MARIMONT, D. H., AND HEEGER, D. 1998. Robust anisotropic diffusion. *IEEE Trans. on Image Processing 7*, 3, 421–432.

CARON, J. N., M., N. N., AND J., R. C. 2002. Noniterative blind data restoration by use of an extracted filter function. *Applied optics (Appl. opt.) 41*, 32, 68–84.

DEY, N., BLANC-FRAUD, L., ZIMMER, C., KAM, Z., ROUX, P., OLIVO-MARIN, J., AND ZERUBIA., J. 2006. Richardson-lucy algorithm with total variation regularization for 3d confocal microscope deconvolution. *Microscopy Research Technique 26*, 69, 260–266.

DOWSKI, E. R., AND JOHNSON, G. E. 1999. Wavefront coding: A modern method of achieving high performance and/or low cost imaging systems. In *SPIE*, vol. 29, 137–145.

Figure 11: *A toy monkey taken by a telephoto lens. From left to right: blurred image and kernel, result by standard RL, and by our approach.*

DURAND, F., AND DORSEY, J. 2002. Fast bilateral filtering for the display of high-dynamic-range images. In *Proceedings of SIGGRAPH*, 257–266.

EISEMANN, E., AND DURAND, F. 2004. Flash photography enhancement via intrinsic relighting. *ACM Trans. on Graph. (SIGGRAPH) 23*, 3, 673–678.

FERGUS, R., SINGH, B., HERTZMANN, A., ROWEIS, S. T., AND FREEMAN, W. T. 2006. Removing camera shake from a single photograph. *ACM Trans. on Graph. (SIGGRAPH) 25*, 3, 787–794.

FIGUEIREDO, M., BIOUCAS-DIAS, J., AND NOWAK, R. 2007. Majorization-minimization algorithms for wavelet-based image restoration. *IEEE Trans. on Image Processing 16*, 12, 2980–2991.

GEMAN, D., AND REYNOLDS, G. 1992. Constrained restoration and the recovery of discontinuities. *IEEE Trans. on PAMI. 14*, 3, 367–383.

GEMAN, D., AND YANG, C. 1995. Nonlinear image recovery with half-quadratic regularization. *IEEE Trans. on Image Processing 4*, 7, 932–946.

GREEN, P., SUN, W., MATUSIK, W., AND DURAND, F. 2007. Multi-aperture photography. *ACM Trans. on Graph. (SIGGRAPH) 26*, 6, 68–75.

INVENSENSE.COM. http://www.invensense.com/.

JIA, J. 2007. Single image motion deblurring using transparency. In *Proceedings of CVPR*, 1141–1151.

KOPF, J., COHEN, M., LISCHINSKI, D., AND UYTTENDAELE, M. 2007. Joint bilateral upsampling. *ACM Trans. on Graph. (SIGGRAPH) 26*, 3, 96–99.

KUNDUR, D., AND HATZINAKOS, D. 1996. Blind image deconvolution. *IEEE Signal Processing Magazine. 13*, 3, 43–64.

LEVIN, A., FERGUS, R., DURAND, F., AND FREEMAN, W. T. 2007. Image and depth from a conventional camera with a coded aperture. *ACM Trans. on Graph. (SIGGRAPH) 26*, 6, 70–77.

LEVIN, A. 2006. Blind motion deblurring using image statistics. In *Advances in Neural Information Processing Systems 19*, 841–848.

LEVOY, M., NG, R., ADAMS, A., FOOTER, M., AND HOROWITZ, M. 2006. Light field microscopy. *ACM Trans. on Graph. (SIGGRAPH) 25*, 3, 68.

LUCY, L. 1974. An iterative technique for the rectification of observed distributions. *Astronomical Journal 79*, 745.

MIGNOTTE, M. 2006. A segmentation-based regularization term for image deconvolution. *IEEE Trans on Image Processing 15*, 7, 1973–1984.

MURTAGH, F., STARCK, J. L., AND BIJAOUI., A. 1995. Image restoration with noise suppression using a multiresolution support. *Astronomy and Astrophysics*, 112, 179–189.

NEELAMANI, R., CHOI, H., AND BARANIUK, R. 2004. ForWaRd: Fourier-wavelet regularized deconvolution for ill-conditioned systems. *IEEE Trans. on Signal Processing 52*, 2, 418–433.

PETSCHNIGG, G., AGRAWALA, M., HOPPE, H., SZELISKI, R., COHEN, M., AND TOYAMA., K. 2004. Digital photography with flash and no-flash image pairs. *ACM Trans. on Graph. (SIGGRAPH) 23*, 3, 664–672.

RASKAR, R., AGRAWAL, A., AND TUMBLIN, J. 2006. Coded exposure photography: motion deblurring using fluttered shutter. *ACM Trans. on Graph. (SIGGRAPH) 25*, 3, 795–804.

REEVES, S. J., AND MERSEREAU, R. M. 1992. Blur identification by the method of generalized cross-validation. *IEEE Trans. on Image Processing. 1*, 3, 301–311.

RUDIN, L., OSHER, S., AND FATEMI, E. 1992. Nonlinear total variation based noise removal algorithms. *Physica D 60*.

TERZOPOULOS, D. 1986. Regularization of inverse visual problems involving discontinuities. *IEEE Trans. on PAMI 8*, 4, 413–242.

TIKHONOV, A. 1943. On the stability of inverse problems. *Dokl. Akad. Nauk SSSR 39*, 5, 195–198.

TOMASI, C., AND MANDUCHI, R. 1998. Bilateral filtering for gray and color images. In *Proceedings of ICCV*, 839–847.

VEERARAGHAVAN, A., RASKAR, R., AGRAWAL, A., MOHAN, A., AND TUMBLIN, J. 2007. Dappled photography: mask enhanced cameras for heterodyned light fields and coded aperture refocusing. *ACM Trans. on Graph. (SIGGRAPH) 26*, 6, 69–76.

YUAN, L., SUN, J., QUAN, L., AND SHUM, H.-Y. 2007. Image deblurring with blurred/noisy image pairs. *ACM Trans. on Graph. (SIGGRAPH) 26*, 3, 1–10.

ZAND, J. 1996. Coded aperture imaging in high energy astronomy. *NASA Laboratory for High Energy Astrophysics (LHEA) at NASA's GSFC*.
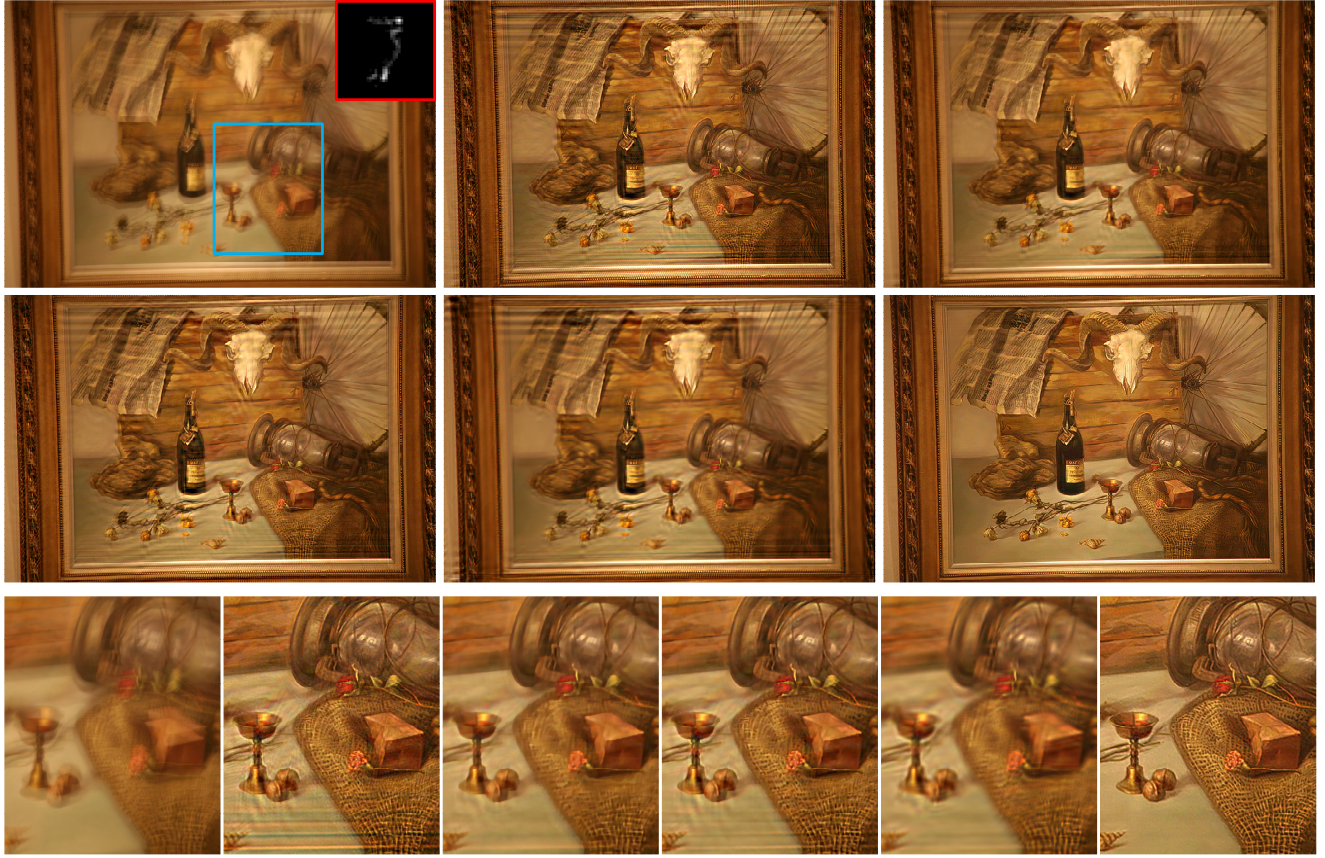
Figure 12: *A painting in the museum. Top (from left to right): blurred image and estimated kernel, standard RL, and TV regularization. Middle (from left to right): Levin's method, wavelet regularization, and our approach. Bottom: close-up views in the lexicographic order.*
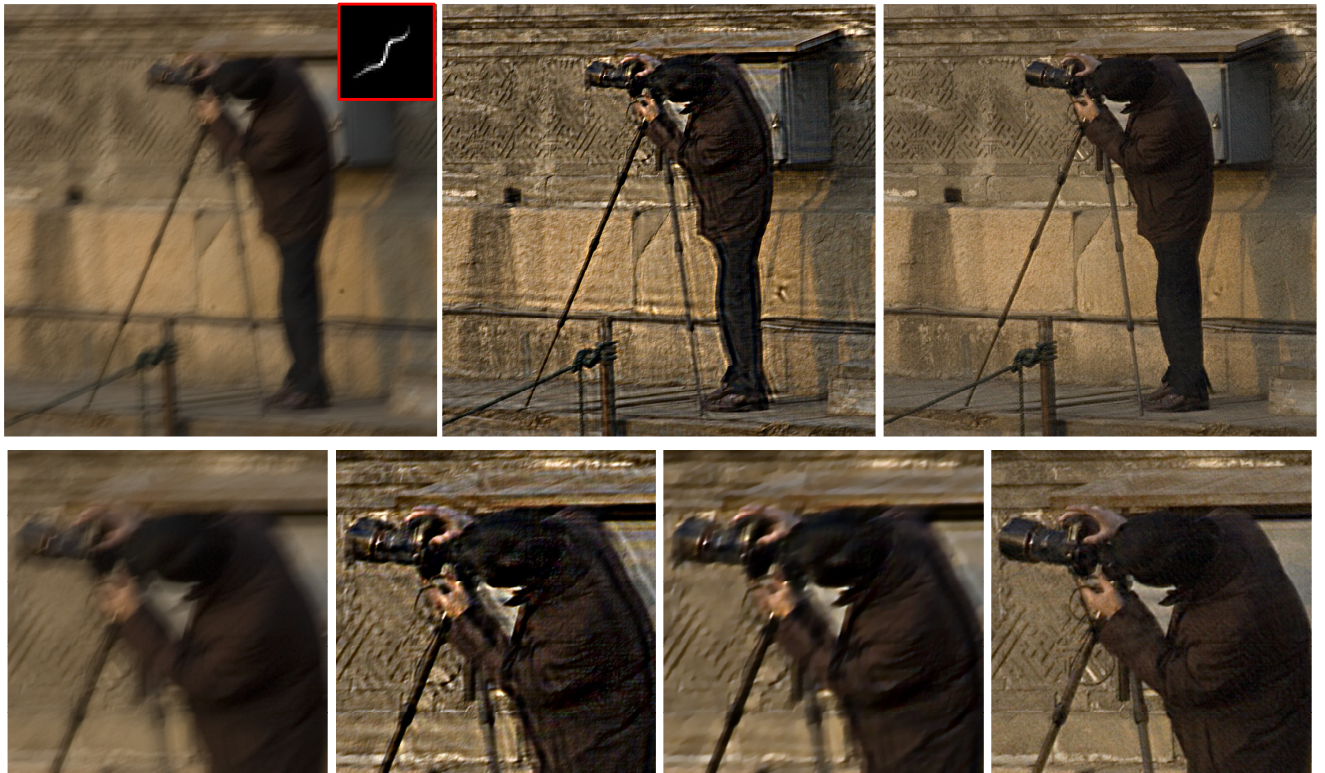
Figure 13: *An outdoor photographer. Top: blurred image and kernel, standard RL, and our approach. Bottom: close-up views of blurred image, standard RL, TV regularization, and our approach.*

(a) blurred image and kernel   (b) [Fergus et al. 2006]   (c) our result   (d) close-up views

(a) blurred image and kernel   (b) [Fergus et al. 2006]   (c) our result   (d) close-up views
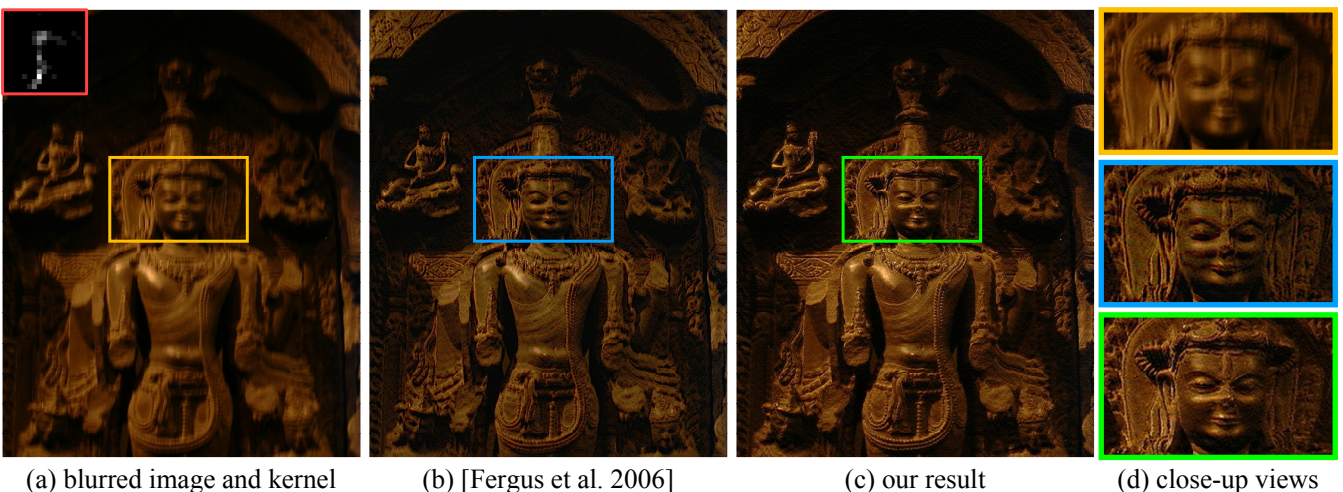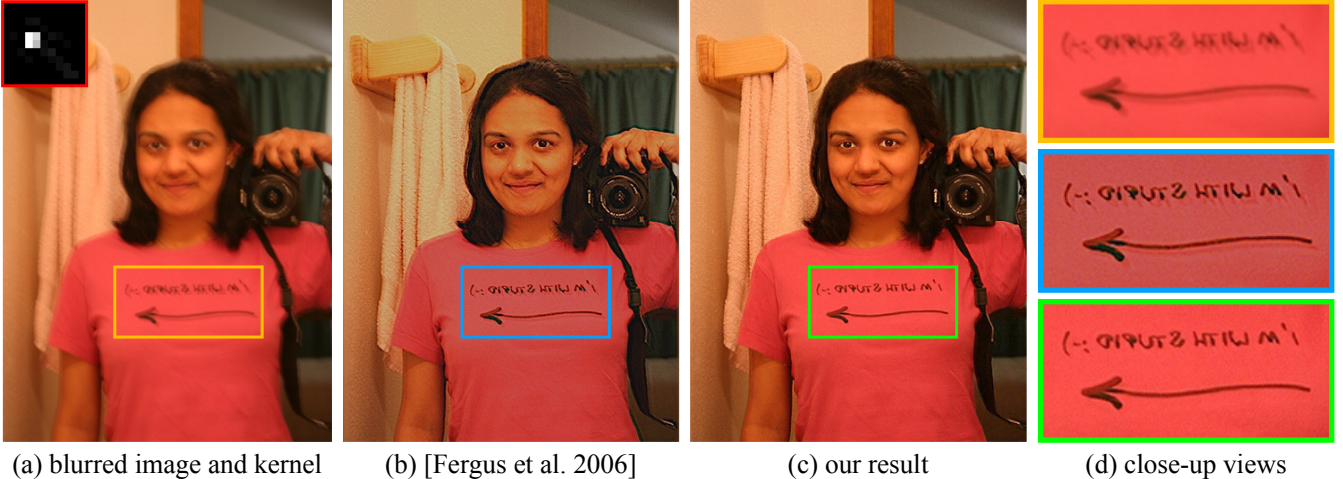
Figure 14: *(a) The input blurred images and estimated kernels are borrowed from [Fergus et al.2006]. (b) Their results (borrowed from [Fergus et al. 2006]) are achieved by a standard RL algorithm given estimated kernel. (c) our decovolution results from the same blurred images and estimated kernels (d) Close-up views show our results contain fewer ringing artifacts and ghosting effects than Fergus et al.'s result.*


(a) blurred image and kernel   (b) [Yuan et al. 2007]   (c) our result   (d) close-up views
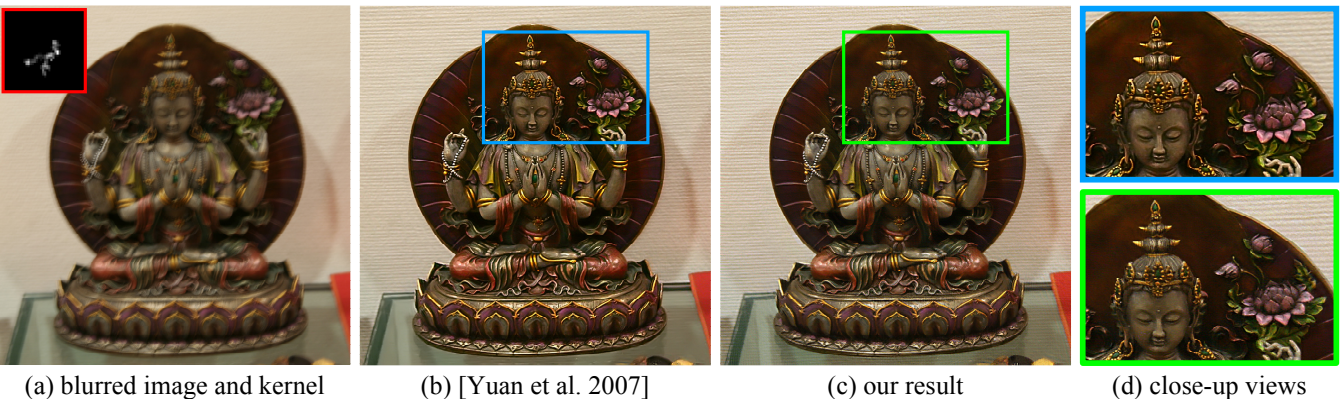
Figure 15: *(a) The input blurred image is borrowed from [Yuan et al. 2007] and the kernel is estimated from the blurred image using [Fergus et al. 2006]. (b) The deconvolution result (borrowed from [Yuan et al. 2007]) is achieved from a pair of images(blurred/noisy). (c) our non-blind deconvolution result is computed from the blurred image only. The kernel is estimated by [Fergus et al. 2006].*